Solis-Tinoco V., Marquez S., Sepulveda B., Lechuga L.M.. Fabrication of well-ordered silicon nanopillars embedded in a microchannel: Via metal-assisted chemical etching: A route towards an opto-mechanical biosensor. RSC Advances, (2016). 6. : 85666 - . 10.1039/c6ra15485a.

Journal Name

ARTICLE

Received 00th January 20xx,
Accepted 00th January 20xx

DOI: 10.1039/x0xx00000x

www.rsc.org/

Fabrication of well-ordered silicon nanopillars embedded in a microchannel via metal-assisted chemical etching: A route towards an opto-mechanical biosensor

V. Solis-Tinoco, [a] S. Marquez, [a] B. Sepulveda [a] and L.M Lechuga [a,*]

Ordered nanopillars have been used as a smart configuration to design and fabricate localized surface plasmon resonance (LSPR) sensors. Importantly, these nanostructures can be integrated within microfluidic channels as a novel opportunity to enhance the response of biosensors and also to control the fluid flow by modifying the wettability surface of the walls. In this work, we demonstrate a large-scale and low-cost nanofabrication methodology that integrates the fabrication of silicon nanopillars (SiNPs) inside a microfluidic channel. The strategy is based on placing a catalytic gold layer patterned with nanoholes inside a SU-8 microchannel,by combining nanosphere lithography, reactive ion etching, and e-beam gold deposition, to control the area, separation distance and diameter of the nanostructures. The height of the SiNPs strongly depends on a well-controlled metal-assisted silicon etching protocol. We demonstrate experimentally that the design and the cleaning of the catalytic gold mesh using ultraviolet ozone strongly affect the etching rate for the formation of large-surface-area nanopillars. Our results explain the fast fabrication of hexagonal arrays of SiNPs embedded in a microfluidic channel with varying aspect ratio from 2 to 7 and separation of 300 nm and 400 nm, respectively, which has important implications for the achievement of new optomechanical biosensors.

Introduction

Nanotechnology has been playing an increasingly important role in the development of new sensor platforms. The use of nanomaterials and the ability to build structures with nano-scale dimensions has enhanced the sensitivity and performance of these sensors. Recently, the use of vertically aligned nanopillars has been proved to be advantageous for developing new sensing devices[1–8]. Particularly, in the emerging field of plasmonics, the configuration of nanopillars has been explored for different applications. For instance, a simple strategy is used for reducing the substrate effect by lifting the enhanced electromagnetic fields of the nanostructures from the substrate by a dielectric pillar, thereby substantially enhancing the bulk refractive index sensitivity of the nanostructure LSPR [9,10]. Similarly, plasmonic metal particles on polymer nanopillars have shown to improve the refractive index sensitivity of LSPR sensors[11–14]. Additionally, the fascinating optical properties of metal nanopillars (e.g. Au and Ag) have been extensively investigated both experimentally and theoretically, providing new pathways for manipulating light at the subwavelength scale, and information for developing new plasmonic applications[15–19]. Also metal (Ag and Au) capped silicon nanopillars are studied to research the impact of the overall geometry of the structures for use as surface-enhanced Raman scattering (SERS) sensors templates[20,21]. Then, one of the challenges in the fabrication of novel plasmonic biosensors based on nanostructures is to create reliable and controllable features with large-area patterns, and subwavelength spatial-resolutions at low-cost and in a reproducible manner. It is widely recognized that the spectral position and magnitude of the LSPR strongly depends on the composition, size, geometry and separation distance of nanostructures as well as in the local dielectric properties of their surrounding environment[9,11,13,22–24]. Hence, reliable techniques and reproducible nanofabrication protocols are needed to create new and cost-effective biosensor platforms compatible with other technologies. Moreover, these protocols must be flexible to identify the parameters, limits, and defects that influence the fabrication of the sensor.

On the other hand, considerable efforts have been made to integrate nanostructures within microfluidic channels to develop competitive sensors given the close interplay of microfluidics with the sensor's technology. For instance, the introduction of well-ordered nanopillar arrays into microfluidic channels has been employed to study the electroosmotic flow suppression during electrophoretic separation[25], or to control the fluid flow by modifying the wettability surface of microchannels[26]. Conventionally, bottom-up and top-down

---

[a] a. Nanobiosensors and Bioanalytical Applications Group, Catalan Institute of Nanoscience and Nanotechnology (ICN2), CSIC and The Barcelona Institute of Science and Technology, Campus UAB, Bellaterra, 08193 Barcelona, Spain

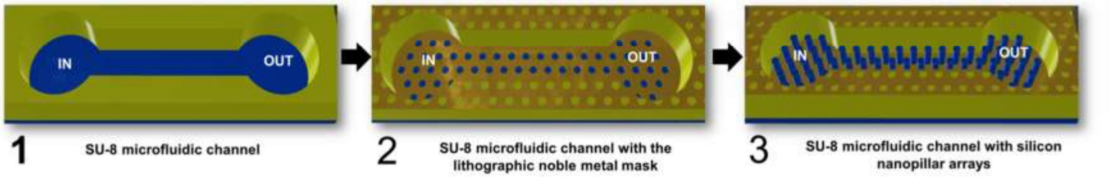

Fig. 1. Overview of the fabrication process of a silicon master mould in order to build a nano-scale sensor

techniques have been employed to produce these microfluidic devices[27] and silicon nanopillars (SiNPs) [28–40]. However, each fabrication technique provides specific characteristics, advantages, and limitations over the control of the fabrication process and over the ability to combine them. It is clear that the choice of the most suitable technique to fabricate a sensor is determined by several factors, such as available technologies and facilities, cost, time, available materials, and fabrication capabilities (e.g desired size of the micro-nanostructures).

Lately, the combination of several nanofabrication techniques such as the Shadow Nanosphere Lithography (SNSL)[39] with reactive ion etching (RIE)[38], thermal evaporation and metal-assisted chemical etching[28,40] has provided intriguing possibilities for fabricating Si nanopillar arrays[39] for several reasons. Firstly, the SNSL technique has been widely used as an effective intermedium for the fabrication of Si nanopillar arrays because the sphere monolayers can easily cover large areas of up to 140 cm^2 at a low cost[39,41,42]. The spheres can be readily self-assembled into single layers to conform a high-quality hexagonal array over a polymer based microfluidic channels. By selecting the initial size of the nanospheres, it is possible to set the distance between the SiNPs, which is an important parameter for replica moulding of soft materials[43,44]. Secondly, the diameter of the nanospheres can be reduced to the desired diameter of the SiNPs by adjusting the RIE time and conditions. Thirdly, the catalytic gold mesh can be defined by depositing functional materials (Au, Ag, Pd, Pt) on top of the etched nanospheres, a process known as lithographic masking. Finally, by combining the mesh design of the nanostructures with the advantages of metal-assisted chemical etching, the length, shape, orientation, and morphology can be controlled[40,45]. In spite of the aforementioned advantages, the combination of these nanofabrication techniques has so far been subject to limitations and defects when producing SiNPs. For instance, an inappropriate change in the periodicity, the presence of some defects, as well as hydrocarbon contamination on the catalytic mesh can strongly influence the etching rate and morphology of SiNPs, producing unstable and inhomogeneous structures. Notably, this can damage not only the reproducibility of the fabrication but also the properties of the final sensor. Thus, a detailed study of the methodology to fabricate a biosensor based on Si nanostructures is highly necessary. To address the fabrication issues mentioned above and to extend the applicability of this strategy to integrate on-chip microfluidics, we provide a low-cost and high-throughput protocol to build well-ordered Si nanopillar arrays into a polymer-based SU-8 microfluidic channel. In this way, the advantages of the integration with the microfluidics in terms of reduced analysis time, reagent consumption, and cost can be exploited. We have performed a study and assessment of the main fabrication techniques used in this methodology which is critical for developing controllable processes to produce high-quality devices. This protocol describes how to fabricate large-scale SiNPs with varying aspect ratios from 2 to 7 and separation distance of 300 nm and 400 nm, using the powerful combination of photolithography, SNSL, RIE, and metal-assisted silicon etching fabrication techniques. Our nanofabrication strategy provides high flexibility to control specific features of the Si nanopillar arrays as is the diameter, height and separation of the nanostructures at the bottom of the microfluidic channel, which is essential for developing new biosensor platforms. In contrast to conventional fabrication methods that integrate microfluidic interconnections after the fabrication of nanostructures[46,47], we have exploited the inert properties of the SU-8 polymer (e.g. resistant to HF/H_2O_2 solution) to outline a microfluidic channel. By using our protocol, we avoid the need to further align the nanopillar structures with microfluidic devices, reducing the chances of damaging their topography and integrity. Our fabrication strategy can be potentially used for the rapid design and fabrication of new optomechanical sensors with integrated microfluidics. Finally, the integrated platform can be used as master mould for replica moulding techniques, suitable for mass production of nanostructured integrated polymer devices for sensing applications.

Experimental

Fabrication of the integrated platform

The fabrication technique is based on the development of a SU-8 microfluidic channel to place SiNPs inside the microchannel. The fabrication process includes three main steps: (1) fabrication of the SU-8 microfluidic channel using photolithography, (2) preparation of the catalytic Au layer inside the channel and (3) fabrication of SiNPs by metal-assisted-chemical etching of silicon. See Fig. 1.

Fabrication of microfluidic channels by photolithography

Materials

Commercially available SU-8 2025 negative epoxy photoresist and a methoxy-2-propanol acetate developer from Microchem Corp were used. Si (100) wafer chips (p-type, 5-10 Ω-cm, Siegert wafer) with 279 µm thickness were employed. The photomask was designed using CorelDRAW X5 and a Süss-Microtech MA 1006 Mask Aligner was used for the UV exposition. The thickness of the layer was measured by a Profilometer KLA-Tencor P15.

Fabrication Process

In order to remove any imperfections that can affect the quality of the spin coating process, the wafer was cleaned as follows. Firstly, the wafer was immersed in boiling piranha solution [H_2O_2: H_2SO_4 1:3] for 1 hr at 80 °C to remove organic residues, rinsed several times with distilled water and dried with air. The Si wafer was then dehydrated in an oven at 200 °C for 30 minutes to improve the adhesion of the SU-8 film. Then a 2.5 ml of SU-8 were dispensed onto the center of the wafer using a syringe. To minimize the presence of bubbles, which is a common problem when depositing SU-8 onto the wafer, the resin was allowed to stand overnight inside the syringe. The wafer was spanned using the parameters shown in Table 1 in order to obtain a thin and uniform layer of about 35 µm. Afterwards, a soft-baked was done to remove solvents and to improve adhesion of layers. This process was performed in three different steps on a hot-plate to avoid film shrinkage: step 1 at 65 °C for 5 minutes, step 2 at 95 °C for 3 minutes and step 3 at 65 °C for 5 minutes.

The microchannel was patterned by soft contact photolithography using an energy dosage of 150 - 215 mJ/cm^2 for 40 s according to the thickness of the SU-8 film (≈35 µm). A post-exposure bake of the wafer improved the crosslinking degree and stabilized the irradiated areas for the subsequent step. The SU-8 resin was developed by immersing the wafer in metroxy-2-propanol acetate for 5 minutes at room temperature, rinsed with isopropanol and dried with air. Finally, a hard bake step was performed at 150 °C for 10 minutes on a contact hot plate to harden the photoresist. The final thickness of the microchannel was measured with a profilometer. Measurements of the resin thickness were taken from 20 samples at 5 different locations across the width of the channel in order to obtain the SU-8 average thickness and standard deviation value (StD). The average thickness was ≈34.08 µm with a StD of 1.59. According to fluid mechanics, the microchannel is designed for a laminar flow with a Reynolds number (dimensionless)[48,49] of 142.

Table 1. Parameters of SU-8 spin coating process for fabrication of the microfluidic channel by photolithography (≈35 µm)

Step	Level 1	Level 2
Speed	600 rpm	3000 rpm
Acceleration	600 rpms^{-1}	600 rpms^{-1}
Time	10 s	40 s

Catalytic gold mask preparation

Materials

Commercially available polystyrene spheres (PS) (carboxyl latex beads, 4%w/v) of 400 nm and 300 nm diameter and ethanol absolute were used to prepare a PS solution (1 ml) at 1:1. Surfactant Triton-100 was also used to compact the monolayer and a Gilson Minipuls 3 Peristaltic Pump was used to drain the water. A plasmalab 80 plus from Oxford instruments was utilised to reduce the diameter of the spheres and an e-beam evaporator (ATC ORION deposition system) was employed to deposit the gold on the Si wafer with the SU-8 microfluidic channel.

Fabrication Process

In our study, a hydrophilic glass petri dish was filled with Mili-Q water and 250 µL of the PS solution were dispensed using a Pasteur pipette to slip the spheres onto the water surface (Fig. 2a). The transfer of the spheres into the container was stopped when the monolayer covered about 90% of the water surface (Fig. 2b). The monolayer was formed by recrystallization after 1.5 hr. Then, the monolayer was compacted and separated from the petri dish walls by inserting a wetted needle with triton X-100 (Fig. 2c). Finally, the Si wafers with the microfluidic channels were submerged into the water and aligned under the PS monolayer. The water was then drained slowly until the monolayer was deposited on the Si wafer with the microchannels and the rest of the water evaporated overnight (Fig. 2d). A scanning electron microscopy (SEM) image of the PS sphere monolayer covering the microfluidic channel is shown in Fig. 3b.

Besides the selection of the sphere size, another advantage offered by the SNSL technique is that the PS spheres can be further tailored by using annealing-induced deformation through temperature or by diameter reduction using RIE treatment. In our study, the PS monolayer was modified by a combination of the aforementioned processes. Thus, the spheres were heated at 100 °C for 15 s on a hot-plate to fix them and to enhance the quality of the PS monolayer (Fig. 3a,b). Meanwhile, the diameter of the spheres was reduced by a RIE treatment (Fig. 3c). The source gas used in the RIE was oxygen at a flow rate of 21 sccm, pressure of 150 mTorr and RF power of 75 W. The diameter of the PS spheres was reduced to the desired value by varying the duration of the etching time (Fig. 3d).

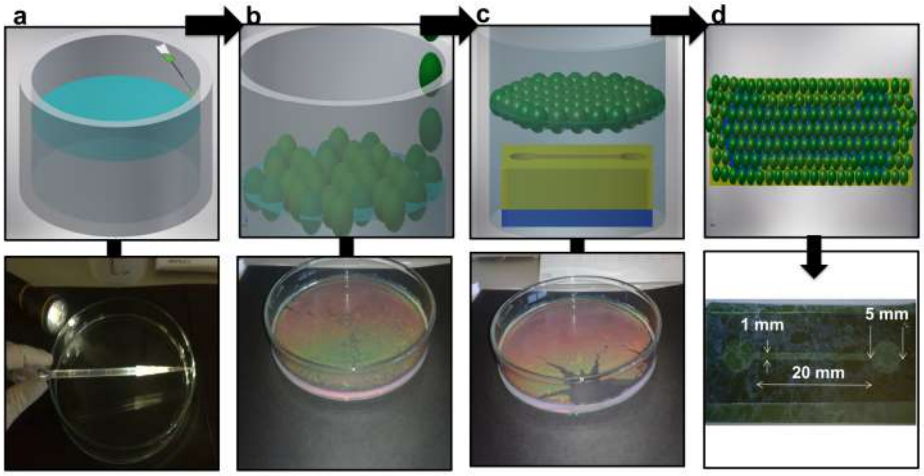

Fig. 2. Schematic illustration and photographs describing the lithography procedure. (a) Position of the Pasteur pipette on the wall of a Petri dish with 13.5 cm of diameter in order to slip the spheres into the water surface. (b) Nanopheres of 400 nm of diameter covering 90% of the water surface. The inset shows the diffraction pattern made upon the illumination of the mask with a lamp. (c) PS monolayer compacted and separated from the glass wall. (d) PS monolayer deposited and adjusted in the SU-8 microchannel.

In metal-assisted chemical etching, gold is one of the most frequently employed noble metals due to its high stability during the chemical etching process, and it can be easily deposited via e-beam evaporation[28,50]. Accordingly, in our study, a titanium film of 0.5 nm thick and a gold film of 19 nm thick were deposited onto the Si wafer surface that contained the microfluidic channels and the etched spheres (Fig. 3d,e). The titanium was used to improve the adhesion of the gold film to the silicon area. Finally, the PS spheres were removed using an ultrasonic bath with ethanol absolute for 1 min, thereby leaving the gold mesh inside the microfluidic channel (Fig. 3f,g). Fig. 3g. clearly shows how the mesh of silicon holes is exposed while the nanospheres are removed. Also, it can be seen the uniformity diameters of silicon holes of the mesh.

Fabrication of Si nanopillars by metal-assisted chemical etching

Materials

A UV-ozone TipCleaner (TM) device was used to remove organic contaminants over the gold mesh of the microchannels and to make the Au and SU-8 surfaces hydrophilic. Hydrogen peroxide (30%), hydrofluoric acid (49%) and deionized water were used as etchant solutions. Four Teflon holders were designed to submerge the microchannels into the chemical solution, and to remove the gold film using potassium iodide (KI).

Working principle

It has been reported that the length of SiNPs fabricated by metal-assisted chemical etching in HF/H_2O_2 solution increases linearly with etching time[51]. In a typical metal-assisted chemical etching procedure, a Si substrate partly covered by a noble metal is subjected to an etchant solution composed of HF and an oxidative agent, typically H_2O_2. The Si beneath the noble metal is etched much faster than the Si without noble metal coverage. As a result, the noble metal sinks into the Si substrate [52], following the widely accepted overall reaction[45]:

$$Si + 6HF + \frac{n}{2}H_2O_2 \rightarrow H_2SiF_6 + nH_2O + \left[\frac{4-n}{2}\right]H_2 \qquad (1)$$

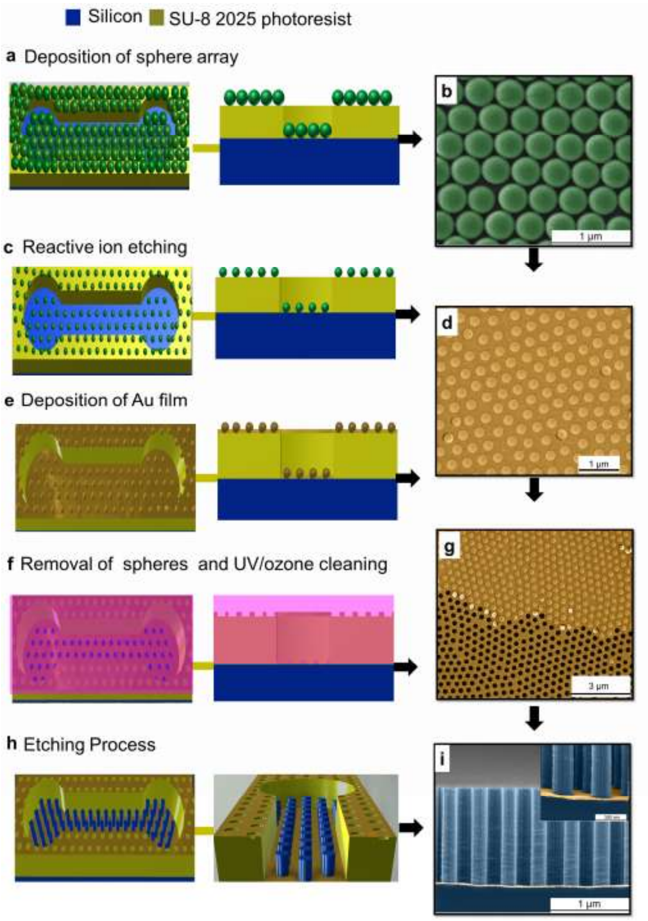

Fig. 3. Schematic illustration of the experimental procedures for fabricating large-area arrays of SiNPs in microfluidic channels. (a) Deposition of PS spheres monolayer in the microfluidic channel. (b) SEM image of a PS sphere monolayer (D = 400 nm) on the microchannel. (c) Reduction in size of the spheres by RIE. (d) SEM image of PS spheres etched by RIE with reduced diameter of 200 nm after an etching time of 100 s. (e) Deposition of Ti and Au layers on the microchannels with reduced spheres. (f) Remove of the spheres by ultrasonication and UV/Ozone cleaning of the gold mask. (g) SEM image of the gold mesh in the microchannel produced when the PS spheres are removed. (h) Cross-sectional scheme of the formation of Si nanopillars in the SU-8 microfluidic channel by catalytic etching. (i) Cross-sectional SEM image of vertically aligned and ordered Si nanopillars in the microfluidic channel produced after 10 min of etching.

Fabrication Process

In order to remove any hydrocarbon contaminant from ambient conditions, the microfluidic channels with the gold mesh were cleaned by ultraviolet (U/V) ozone for 20 minutes to produce clean, hydrophilic and oxidized surfaces[53,54]. The microchannels were then rinsed with isopropanol (15 minutes), in order to slightly reduce the hydrophilicity and activation of the Au layer, and dried with N_2 (Fig. 3f,g). Afterwards, for the fabrication of SiNPs by metal-assisted chemical etching, the Si wafers with microchannels were placed in Teflon holders and immersed simultaneously in an etching mixture consisting of (HF(49%):H_2O_2 (30%):H_2O=6:1:26:v: v: v) at room temperature. The etching duration was varied from 2 to 10 minutes, depending on the desired length of the Si nanopillars.

The etching process was stopped by removing the wafers from the chemical solution and immersing them in distilled water for 20 minutes (Fig. 3h,i). Thereafter, the wafers were immersed in KI solution for 2 minutes to remove the gold film, and rinsed with distilled water (15 minutes) and with isopropanol to minimize capillary effects during N_2 drying.

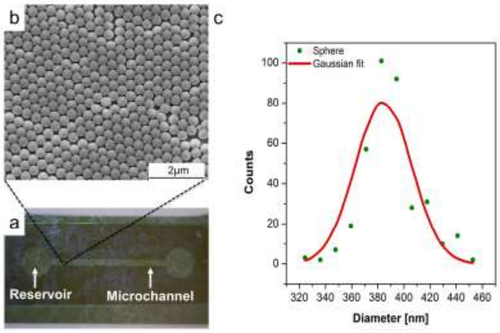

Fig. 4. PS 400 nm monolayer at the bottom of a SU-8 microfluidic channel fabricated by SNSL. (a) Photo showing the PS mask covering the entire SU-8 microfluidic channel. (b) SEM image of the PS sphere array in the SU-8 microfluidic channel, where some defects can be observed (top view, scale bar =2 µm). (c) Size distribution of spheres with diameters with a mean value of 390.04 ± 26.16 nm.

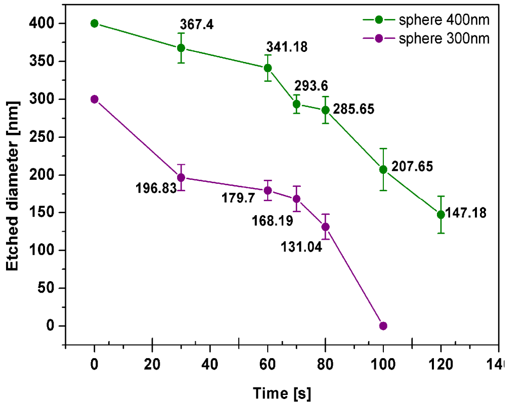

Fig. 5. PS spheres in microfluidic channels etched by RIE with a flow of 21%, 75 W and 150 mTorr. Data plotted on the basis of measurements acquired from SEM images of the reduced diameters of PS spheres of 300 nm and 400 nm of diameter during 120 s of RIE.

Results and discussion

Hexagonal arrangement of Silicon Nanopillars

Fig. 4a shows the final monolayer obtained by the recrystallization of spheres with ≈400 nm in diameter. The monolayer was deposited and adjusted on the area of the microfluidic channel covering it completely (Fig. 4a). The SEM image in Fig. 4b clearly shows the hexagonal array of PS spheres homogenously distributed. Defects in the monolayer such as disorders in the hexagonal arrangement of PS spheres (Fig. 4b,c) and overlapping were transferred into the Si nanopillars array. These defects could be further reduced by improving the control of the sphere deposition to form the monolayer on the water surface and by compacting the spheres. Moreover, other imperfections resulted from differences in size of the initial spheres. Fig. 4c shows the distribution of the diameters of the spheres of 400 nm. The mean diameter of the sphere was 390.04 ± 26.16 nm which matched well with the size provided by the company (390 nm).

Diameter of the Silicon Nanopillars: Etched polystyrene mask within microfluidic channels by RIE

We used the RIE etching process to set the diameter of the SiNPs. The spheres deposited on the microfluidic channel were etched by RIE with oxygen for a period of 30-120 s. SEM images were taken at 4 different locations of the rectangular area of the microchannel (Fig.4a), left, right, up and down to check the results. Fig. 5 shows the reduced diameter of the 300 nm and 400 nm PS spheres according to RIE time. While the RIE of both PS 300 nm and PS 400 nm increased over time, the reduction of the PS 300 nm spheres was faster. At 100 s, the 300 nm spheres were completely etched, whereas the diameter of the 400 nm spheres was reduced to ≈207.65 nm. According to our experiments, excessive RIE time can affect the quality and arrangement of the reduced nanospheres, producing imperfect SiNPs (Fig.6). The differences in diameter values can be explained by the variations in size of the original spheres (Fig. 4c) and by the quality of the equipment used in the RIE treatment.

Height of Silicon Nanopillars

Effect of UV/ozone on the etching process

We found that the cleaning of gold mesh in the microchannels by UV/ozone strongly influenced the etching process. In order to demonstrate this effect eight samples with a gold mesh placed at the bottom of the hydrophobic SU-8 microchannel (contact angle 102.2 ± 0.19°) were used. Their reduced diameters (dr) were kept at ≈280 nm with a center-to-center distance (dcc) of 400 nm. Four samples were then exposed to UV/ozone for 30 minutes to remove the contaminants from the wafer surface and to produce a clean, hydrophilic and oxidized gold mesh in the SU-8 microchannels. Afterwards, the samples were immersed simultaneously in an etching mixture consisting of (HF (49%): H_2O_2 (30%):H_2O=6:1:26:v:v:v) at room temperature. The etching duration was varied from 2 to 8 minutes. Figs. 7a,b shows the SEM images of the structural changes observed in the SiNPs with and without UV/ozone treatment with respect to the etching time.

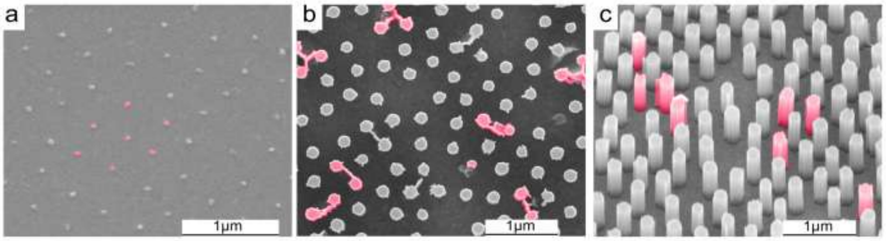

Fig. 6. Defects presented during the nanofabrication of SiNPs. (a) PS 400 nm monolayer in a SU-8 microfluidic channel damaged by an excessive RIE time of 145 s where the nanospheres lost quality in the spherical shape and order (top view, scale bar= 1 µm). (b, c) Top view of deformed SiNPs produced by an excessive time of RIE of 120 s. (c) Imperfect hexagonal arrays of SiNPs caused by defects in the PS monolayer and by an inadequate RIE treatment.

Particularly, Fig. 7b clearly shows that the etching process was slow in samples that were not cleaned with UV/ozone, and as a result, the heights of SiNPs were shorter than those samples subjected to UV/ozone cleaning. This can be explained by considering the contaminant residues on the gold mesh surface, which reduced its quality and delayed the etching reactions (1). The UV/ozone treatment removed contaminants from sample surfaces and produced hydrophilic and oxidized gold mesh in the microchannels that resulted in an accelerated etching rate. Moreover, the SiO_2 monolayer formed in the Si holes of the mesh did not affect the reaction as it was dissolved by HF according to the chemical reaction in (1). Throughout the process, the morphology and quality of the SiNPs were not affected. Importantly, this simple cleaning step avoids the necessity to change the etchant concentration, the type of metal or to increase the temperature to accelerate the etching rate[45]. SEM images were taken to perform a visual characterization of samples at different locations to obtain the average height and the StD value. The temporal evolution of the SiNPs growth inside the SU-8 microfluidic channels is shown in Fig. 7c. According to the graph, an increase of SiNP height with etching time was obtained in both conditions. It can also be observed that the heights of the SiNPs fabricated in the contaminated samples were 100%, 92%, 87% and 71% shorter than the heights of the SiNPs fabricated in the cleaned samples. Therefore, by controlling this factor, a successful fabrication of SiNPs with heights under and over 500 nm can be achieved at the same etching times, clearly demonstrating the influence of UV/ozone cleaning on the fabrication of the SiNPs.

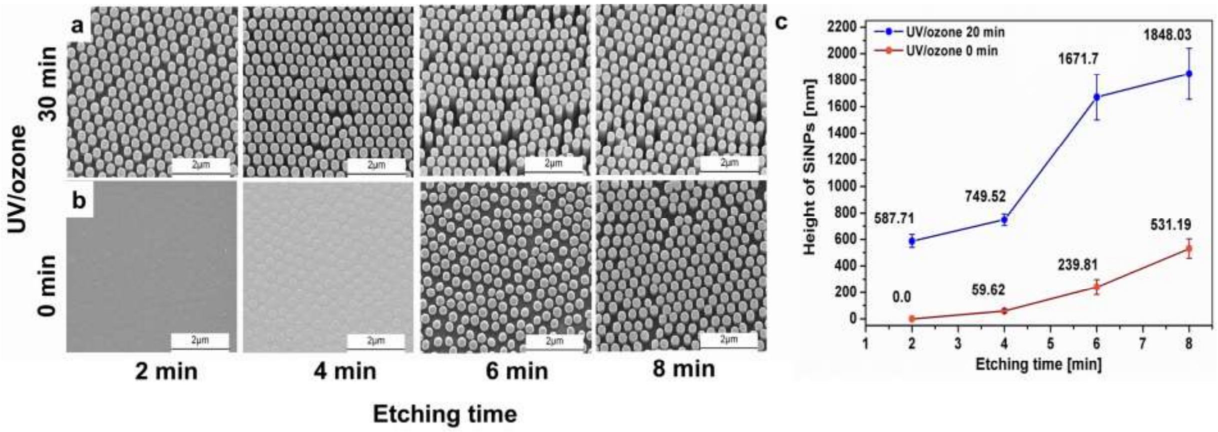

Fig. 7. Effect of the UV/Ozone treatment on the temporal evolution of SiNPs at different etching times. Their diameters were kept at ≈280 nm with a center-to-center distance of 400 nm inside the microfluidic channels during the metal-assisted chemical etching (HF (49%): H_2O_2 (30%):H_2O=6:1:26:v:v:v). Each row indicates the time that the samples were exposed to UV/ozone: (a) 30 min and (b) 0 minutes. Each column indicates the etching time of 2, 4, 6 and 8 minutes, respectively (15° tilt view, scale bar=2 µm). (c) Effect of UV/Ozone on the temporal evolution of the height of the SiNPs in the SU-8 microfluidic channels and the etching time 2, 4, 6 and 8 minutes, respectively, at 0 and 30 minutes of UV/ozone. In both graphs an approximately linear relationship between the heights and etching times was obtained when the etching rate increased with UV/ozone, demonstrating its influence on the etching rate.

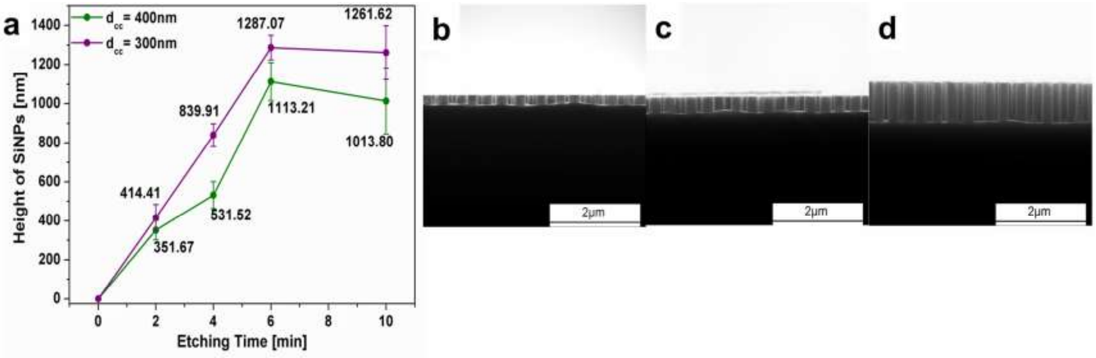

Fig. 8. Temporal evolution of the Si nanopillar heights in the SU-8 microfluidic channels during the etching process. (a) Average heights of the SiNPs separated at a center-to-center distance (dcc) of 300 nm and 400 nm for 2, 4, 6 and 10 minutes, respectively. Cross-sectional SEM images of SiNPs inside the SU-8 microfluidic channels using PS 400 nm spheres with a reduced diameter of 280 nm. The etching times were for (b) 1, (c) 2, and (d) 5 minutes with heights of ≈ 180 nm, ≈300 nm and ≈750 nm, respectively according to the measurements obtained by SEM images.

Controlled fabrication of SiNPs within SU-8 microfluidic channels

To demonstrate the controllability and reproducibility of our nanofabrication method to create embedded nanostructures in polymer microfluidics, another series of experiments were performed. Fig. 8a shows the temporal evolution of the SiNPs fabricated inside microfluidic domains using two different designs of the catalytic gold mesh, prepared with both PS 300 nm and PS 400 nm spheres, with a dr of ≈180 nm and ≈160 nm, respectively. The microchannels were etched in the same solution ((HF (49%): H_2O_2 (30%):H_2O=6:1:26:v:v:v)) for different times of 2, 4, 6 and 10 minutes, respectively. The results confirmed that in the two different catalytic meshes, the height of SiNPs increases as the etching time becomes longer.

Additionally, the graph shows that the design of the catalytic Au mesh with respect to the diameter of the mask holes, the periodicity (d_{cc}=300, d_{cc}=400) and the hexagonal array, influenced as well the etching rate. It can also be observed that the heights of the SiNPs (d_r 180 nm) separated at a d_{cc} of 300 nm were higher than the heights of the SiNPs (d_r =160 nm) separated at a d_{cc} of 400 nm. This can be explained by the fact that the area with the gold/silicon interface in the mesh with the d_r=180 nm and d_{cc}=300 is smaller than in the mesh with the d_r=160 nm and d_{cc}=400, then it sinks faster into the silicon than the other following the reaction (1), thereby producing higher SiNPs[28]. It demonstrates that the combination of d_r and d_{cc}, plays a key role to control the etching rate. Interestingly, after 6 minutes, the etching rate began to stabilize in both cases. To prove the high control of our protocol over the formation of SiNPs, three samples were etched during 1, 2 and 5 minutes, maintaining the same d_{cc} at 400 nm, but now with a d_r=280 nm. Fig. 8b-d indicates the cross-sectional images of the SiNPs in the microchannel. The resulting heights were ≈180 nm, ≈300 nm, and ≈750 nm, respectively, which were the expected values according to the results described in Fig. 8a. Finally, Table 2 shows the mean and StD values of the heights of the fabricated SiNPs. The column %StD represents the percentage of standard deviation with respect to the heights mean value. In both fabrications, there was a controlled and proportional increase in the aspect ratio, and the %StD did not exceed 17%, which was acceptable for our purposes of fabrication.

Table 2. Characteristics of heights of SiNPs using mesh of silicon nanoholes separated 300 nm and 400 nm in the SU-8 microfluidic channels

Etching time	d_r= 180 nm , dcc=300 nm [a], Height [nm] [b]	Aspect ratio (H/dr)[c]	% StD [d]	d_r= 160 nm, dcc=400nm [a] Height [nm] [b]	Aspect ratio (H/dr)[c]	% StD [d]
2	414.41±68.99	2.30	16.64	351.67±49.47	2.19	14.06
4	839.91±58.44	4.66	6.95	531.52±69.37	3.32	13.05
6	1287.07±62.83	7.15	4.88	1113.21±96.93	6.95	8.70
10	1261.62±136.90	7.00	10.85	1013.80±169.08	6.33	16.67

[a] dcc= center to center distance of nanopillars
[b] mean ± standard deviation of 3 replicates of the experiment
[c] H/d_r =Height / reduced diameter
[d] %StD represents the percentage of Std with respect to mean value

Conclusions

We have described a simple and low-cost fabrication protocol of ordered arrays of silicon nanopillars with integrated polymer microfluidics. With our fabrication strategy, the area, hexagonal arrangement, diameter, and height of the SiNPs within the microchannel are well controlled. In this process, it was shown that the diameter of the PS spheres (300 nm and 400 nm of diameter) was reduced by RIE treatment and these results were used to control the diameter of the SiNPs. Explanation and advice were given on how to reduce defects and imperfections in the fabrication of the microchannel and the catalytic gold mesh. Our investigation confirmed that the height of SiNPs increases as the etching time becomes longer. Moreover, the simple cleaning of the microchannels by UV/Ozone clearly affects the etching rate. Importantly, this step avoids the necessity to change the etchant concentration, the type of metal or to increase the temperature to accelerate the etching rate. Through our results, we demonstrate that the combination of reduced diameter (d_r), and periodicity (d_{cc}) of the catalytic gold mesh plays a key role to control the etching rate. The results from our strategy offer a controlled tool for the creation of new optomechanical biosensors integrated in microfluidic devices.

Acknowledgments

V. Solis-Tinoco & S. Marquez acknowledge financial support from ¨Programa becas en el extranjero¨ from National Council for Science and Technology (CONACyT-Mexico). The nanoB2A is a consolidated research group (Grup de Recerca) of the Generalitat de Catalunya and has support from the Departament d'Universitats, Recerca i Societat de la Informació de la Generalitat de Catalunya (2014 SGR 624). ICN2 is the recipient of Grant SEV-2013-0295 from the "Severo Ochoa Centers of Excellence" Program of Spanish MINECO. We acknowled financial support of MINECO, projects FIS2013-49280-EXP, MAT2011-12645-E.

References

1 A. Gin, B. Movaghar, M. Razeghi and G. J. Brown, *Nanotechnology*, 2005, **16**, 1814–1820.
2 L.-J. Bie, X.-N. Yan, J. Yin, Y.-Q. Duan and Z.-H. Yuan, *Sens. Actuators B Chem.*, 2007, **126**, 604–608.
3 V. Anandan, X. Yang, E. Kim, Y. L. Rao and G. Zhang, *J. Biol. Eng.*, 2007, **1**, 5.
4 C. Wang, M. Hossain, L. Ma, Z. Ma, J. J. Hickman and M. Su, *Biosens. Bioelectron.*, 2010, **26**, 437–443.
5 Y. Suzuki and K. Yokoyama, *Biosens. Bioelectron.*, 2011, **26**, 3696–3699.
6 M. Holgado, C. A. Barrios, F. J. Ortega, F. J. Sanza, R. Casquel, M. F. Laguna, M. J. Bañuls, D. López-Romero, R. Puchades and A. Maquieira, *Biosens. Bioelectron.*, 2010, **25**, 2553–2558.
7 H. S. Wasisto, S. Merzsch, A. Stranz, A. Waag, E. Uhde, T. Salthammer and E. Peiner, *Procedia Eng.*, 2012, **47**, 289–292.
8 V. Anandan, Y. L. Rao and G. Zhang, *Int. J. Nanomedicine*, 2006, **1**, 73–79.
9 M. A. Otte, M.-C. Estévez, L. G. Carrascosa, A. B. González-Guerrero, L. M. Lechuga and B. Sepúlveda, *J. Phys. Chem. C*, 2011, **115**, 5344–5351.
10 A. Dmitriev, C. Hägglund, S. Chen, H. Fredriksson, T. Pakizeh, M. Käll and D. S. Sutherland, *Nano Lett.*, 2008, **8**, 3893–3898.
11 W. Knoben, S. H. Brongersma and M. Crego-Calama, *Nanotechnology*, 2011, **22**, 295303.
12 Y. Shen, J. Zhou, T. Liu, Y. Tao, R. Jiang, M. Liu, G. Xiao, J. Zhu, Z.-K. Zhou, X. Wang, C. Jin and J. Wang, *Nat. Commun.*, 2013, **4**.
13 M. Saito, A. Kitamura, M. Murahashi, K. Yamanaka, L. Q. Hoa, Y. Yamaguchi and E. Tamiya, *Anal. Chem.*, 2012, **84**, 5494–5500.
14 S.-C. Yang, J.-L. Hou, A. Finn, A. Kumar, Y. Ge and W.-J. Fischer, *Nanoscale*, 2015, **7**, 5760–5766.
15 H. Zheng, R. Vallée, I. Ly, R. M. Almeida, T. Rivera and S. Ravaine, *J. Phys. Chem. C*, 2015.
16 G. Si, X. Jiang, J. Lv, Q. Gu and F. Wang, *Nanoscale Res. Lett.*, 2014, **9**, 299.
17 K. Wang and K. B. Crozier, *ChemPhysChem*, 2012, **13**, 2639–2648.
18 A. E. Çetin, A. A. Yanik, C. Yilmaz, S. Somu, A. Busnaina and H. Altug, *Appl. Phys. Lett.*, 2011, **98**, 111110.
19 W. Kubo and S. Fujikawa, *Nano Lett.*, 2011, **11**, 8–15.
20 M. S. Schmidt, J. Hübner and A. Boisen, *Adv. Mater.*, 2012, **24**, OP11-OP18.
21 J. D. Caldwell, O. Glembocki, F. J. Bezares, N. D. Bassim, R. W. Rendell, M. Feygelson, M. Ukaegbu, R. Kasica, L. Shirey and C. Hosten, *ACS Nano*, 2011, **5**, 4046–4055.
22 T. R. Kaiyu Wu, *Opt. Express*, 2015, **23**, 12965–12978.
23 B. Sepúlveda, P. C. Angelomé, L. M. Lechuga and L. M. Liz-Marzán, *Nano Today*, 2009, **4**, 244–251.
24 M.-C. Estevez, M. A. Otte, B. Sepulveda and L. M. Lechuga, *Anal. Chim. Acta*, 2014, **806**, 55–73.
25 T. Yasui, N. Kaji, M. R. Mohamadi, Y. Okamoto, M. Tokeshi, Y. Horiike and Y. Baba, *ACS Nano*, 2011, **5**, 7775–7780.
26 T. Wang, H. Chen, K. Liu, Y. Li, P. Xue, Y. Yu, S. Wang, J. Zhang, E. Kumacheva and B. Yang, *Nanoscale*, 2014, **6**, 3846–3853.

27 F. Gina S and D. T. Chiu, *BioTecniques*, 2005, **38**.
28 M. A. Otte, V. Solis-Tinoco, P. Prieto, X. Borrisé, L. M. Lechuga, M. U. González and B. Sepulveda, *Small*, 2015, n/a-n/a.
29 H. Sato, Y. Houshi and S. Shoji, *Microsyst. Technol.*, 2004, **10**, 440–443.
30 J. Fujita, M. Ishida, T. Ichihashi, Y. Ochiai, T. Kaito and S. Matsui, *Nucl. Instrum. Methods Phys. Res. Sect. B Beam Interact. Mater. At.*, 2003, **206**, 472–477.
31 J. Westwater, *J. Vac. Sci. Technol. B Microelectron. Nanometer Struct.*, 1997, **15**, 554.
32 L. Schubert, P. Werner, N. D. Zakharov, G. Gerth, F. M. Kolb, L. Long, U. Gösele and T. Y. Tan, *Appl. Phys. Lett.*, 2004, **84**, 4968.
33 J. Bauer, F. Fleischer, O. Breitenstein, L. Schubert, P. Werner, U. Gösele and M. Zacharias, *Appl. Phys. Lett.*, 2007, **90**, 12105.
34 J. L. Liu, S. J. Cai, G. L. Jin, S. G. Thomas and K. L. Wang, *J. Cryst. Growth*, 1999, **200**, 106–111.
35 Y.-H. Yang, S.-J. Wu, H.-S. Chiu, P.-I. Lin and Y.-T. Chen, *J. Phys. Chem. B*, 2004, **108**, 846–852.
36 L. C. Tien, S. J. Pearton, D. P. Norton and F. Ren, *J. Mater. Sci.*, 2008, **43**, 6925–6932.
37 A. Umar and Y. B. Hahn, *Appl. Phys. Lett.*, 2006, **88**, 173120.
38 Y.-F. Chang, Q.-R. Chou, J.-Y. Lin and C.-H. Lee, *Appl. Phys. A*, 2006, **86**, 193–196.
39 J. Zhang, Y. Li, X. Zhang and B. Yang, *Adv. Mater.*, 2010, **22**, 4249–4269.
40 N. Geyer, B. Fuhrmann, Z. Huang, J. de Boor, H. S. Leipner and P. Werner, *J. Phys. Chem. C*, 2012, **116**, 13446–13451.
41 L. Li, T. Zhai, H. Zeng, X. Fang, Y. Bando and D. Golberg, *J. Mater. Chem.*, 2010, **21**, 40–56.
42 A. Kosiorek, W. Kandulski, P. Chudzinski, K. Kempa and M. Giersig, *Nano Lett.*, 2004, **4**, 1359–1363.
43 D. J. Lipomi, M. A. Kats, P. Kim, S. H. Kang, J. Aizenberg, F. Capasso and G. M. Whitesides, *ACS Nano*, 2010, **4**, 4017–4026.
44 V. Solis-Tinoco, B. Sepulveda and L. M. Lechuga, 2015, vol. 9519, p. 95190T–95190T–9.
45 Z. Huang, N. Geyer, P. Werner, J. de Boor and U. Gösele, *Adv. Mater.*, 2011, **23**, 285–308.
46 C. Gonzalez, S. D. Collins and R. L. Smith, in *, 1997 International Conference on Solid State Sensors and Actuators, 1997. TRANSDUCERS '97 Chicago*, 1997, vol. 1, pp. 527–530 vol.1.
47 B. Zhang, Q. Dong, C. E. Korman, Z. Li and M. E. Zaghloul, *Sci. Rep.*, 2013, **3**.
48 R. W. R. L. Gajasinghe, S. U. Senveli, S. Rawal, A. Williams, A. Zheng, R. H. Datar, R. J. Cote and O. Tigli, *J. Micromechanics Microengineering*, 2014, **24**, 75010.
49 S. K. Sia and G. M. Whitesides, *ELECTROPHORESIS*, 2003, **24**, 3563–3576.
50 Z. R. Dai, Z. W. Pan and Z. L. Wang, *Adv. Funct. Mater.*, 2003, **13**, 9–24.
51 Z. Huang, H. Fang and J. Zhu, *Adv. Mater.*, 2007, **19**, 744–748.
52 C. Chartier, S. Bastide and C. Lévy-Clément, *Electrochimica Acta*, 2008, **53**, 5509–5516.
53 D. E. King, *J. Vac. Sci. Technol. A*, 1995, **13**, 1247–1253.
54 M. T. Lee M. Fischer, *Microelectron. Eng.*, 2009, **86**, 1282–1285.